AIP Advances

Hybrid integration of carbon nanotube and amorphous IGZO thin-film transistors

Cite as: AIP Advances **10**, 025131 (2020); https://doi.org/10.1063/1.5139085
Submitted: 18 November 2019 . Accepted: 03 February 2020 . Published Online: 20 February 2020

Yongwoo Lee, Jinsu Yoon, Jun Tae Jang, Bongsik Choi, Hyo-Jin Kim, Geon-Hwi Park, Dong Myong Kim, Dae Hwan Kim, Min-Ho Kang, and Sung-Jin Choi

Hybrid integration of carbon nanotube and amorphous IGZO thin-film transistors

Cite as: AIP Advances 10, 025131 (2020); doi: 10.1063/1.5139085
Submitted: 18 November 2019 • Accepted: 3 February 2020 •
Published Online: 20 February 2020

Yongwoo Lee,[1] Jinsu Yoon,[1] Jun Tae Jang,[1] Bongsik Choi,[1] Hyo-Jin Kim,[1] Geon-Hwi Park,[1] Dong Myong Kim,[1] Dae Hwan Kim,[1] Min-Ho Kang,[2,a)] and Sung-Jin Choi[1,b)]

AFFILIATIONS

[1]School of Electrical Engineering, Kookmin University, Seoul 02707, South Korea
[2]Department of Nano-process, National Nanofab Center (NNFC), Daejeon 34141, South Korea

[a)]**Electronic mail:** kmh@nnfc.re.kr. **Tel.:** +82-2-910-5543. **Fax**: +82-2-910-4449
[b)]**Author to whom correspondence should be addressed:** sjchoiee@kookmin.ac.kr

ABSTRACT

Solution-processed carbon nanotubes (CNTs) have recently attracted significant attention as *p*-type thin-film transistor (TFT) channels due to their high carrier mobility, high uniformity, and low process temperature. However, implementing sophisticated macroelectronics with a combination of single CNT-TFTs has been challenging because it is difficult to fabricate *n*-type CNT-TFTs. Therefore, in combination with indium-gallium-zinc-oxide (IGZO), which has excellent electrical performance and has been commercialized as an *n*-type oxide TFT, we demonstrated various hybrid complementary metal-oxide semiconductor integrated circuits, such as inverters and NOR and NAND gates. This hybrid integration approach allows us to combine the strength of *p*-type CNT- and *n*-type IGZO-TFTs, thus offering a significant improvement for macroelectronic applications.

High-performance flexible electronics are highly desirable for wearable, medical, healthcare, and robotics applications.[1–3] Carbon nanotubes (CNTs) are promising candidates for high-performance flexible electronics due to their high carrier mobility, high current density, high mechanical flexibility/stretchability, and compatibility with printing processes.[4–8] In particular, highly purified semiconducting CNTs have attracted widespread attention for manufacturing diodes, field-effect transistors (FETs), thin-film transistors (TFTs), and integrated circuit (IC) applications.[9–12] In addition, TFTs with record-breaking performance have been reported using CNTs achieved from a density-gradient ultracentrifugation method, with semiconducting purity above 99%.[13] However, CNT-TFTs typically exhibit *p*-type properties under ambient conditions due to the adsorption of oxygen and water vapor;[14–16] therefore, if the ICs are implemented with only CNTs, they are expected to exhibit poor electrical performance. There have been many efforts to convert *p*-type operations to *n*-type operations,[17–20] but controllability and stability issues remain difficult to resolve. To overcome the aforementioned issues, new concepts of CNT-based IC applications, such as pseudocomplementary metal-oxide semiconductor (CMOS) combination circuits and diode-based circuits, have been demonstrated.[21,22] Nevertheless, complex process steps, low integration, and high manufacturing costs remain.

Recently, as interest in macroelectronic circuits with low static power consumption has increased, hybrid combinations of complementary materials such as CNTs and amorphous indium-gallium-zinc-oxide (IGZO) have widely been studied for various complementary circuits.[16,23–25] IGZO is one of the most promising members in the amorphous oxide semiconductor category, with excellent *n*-type electrical performance.[26,27] In particular, IGZO-based TFTs have been successfully employed in pixel driving circuits, such as liquid crystal displays (LCDs) and organic light emitting diodes (OLEDs), for commercial display applications.[28]

Here, we demonstrate a hybrid integration based on *p*-type CNT-TFTs and *n*-type IGZO-TFTs to achieve hybrid CMOS ICs, which are a potential candidate to replace silicon CMOS technology. We evaluated the electrical performances of devices (CNT- and IGZO-TFTs) and ICs (inverters and NAND and NOR gates). The fabricated CNT- and IGZO-TFTs showed high on-state current (I_{ON}), high on/off current ratio [$\log(I_{ON}/I_{OFF})$], and high carrier

mobility (μ_{FE}). By employing these TFTs, the hybrid CMOS inverters exhibited excellent electrical performances with low power consumption and high voltage gains. Finally, we also demonstrate the operations of the two-input NAND and NOR gates fabricated based on the CNT- and IGZO-TFTs. As a result, the logic circuits provide correct logical functions according to input signals. We believe that the hybrid integration approach combines the strength of *p*-type CNT- and *n*-type IGZO-TFTs for high-performance CMOS IC designs.

Figure 1(a) illustrates the details of the fabrication processes of a hybrid CMOS inverter based on the CNT- and the IGZO-TFTs, and the two-input NAND and NOR gates also have the same process steps. First, the hybrid device fabrication was initiated on a silicon (Si) wafer with a thermally grown 300-nm-thick silicon dioxide (SiO_2) layer. Next, the titanium (Ti) local bottom gate with a thickness of 20 nm was deposited with an electron-beam (e-beam) evaporator. An aluminum oxide (Al_2O_3) with a thickness of 40 nm was grown as a gate insulator through atomic layer deposition (ALD) at 80 °C, and then, a 10-nm-thick SiO_2 layer was formed using e-beam evaporation for effective semiconducting CNT network formation. At present, the formation of the bottom gate and gate insulator is the same process for *p*-type CNT- and *n*-type IGZO-TFTs. To fabricate the *p*-type CNT-TFT, the surface of the SiO_2 layer was first cleaned by oxygen plasma treatment for 1 min at 30 W. The substrate was functionalized with a poly-L-lysine solution (0.1% w/v in water; Sigma Aldrich) by dropping the solution onto the SiO_2 surface to introduce an amine-terminated adhesion layer for the efficient deposition of the CNT percolated network,[29,30] followed by rinsing with de-ionized (DI) water. Subsequently, to deposit the semiconducting CNT network, the substrate was immersed into a commercially available 0.01 mg/ml 99% semiconducting CNT solution (purchased from NanoIntegris, Inc.) for 20 min with elevated temperature at 100 °C and was thoroughly rinsed with DI water and isopropanol. Afterward, the *p*-type CNT source and drain (S/D) electrodes consisting of Ti and palladium (Pd) layers (each 2 nm and 30 nm, respectively) were formed using e-beam evaporation and a lift-off process. Next, to define the percolated CNT network channel, additional photolithography and an oxygen plasma-etching process were conducted to remove unwanted electrical paths, which isolated the devices from one another. Thus, the fabrication of the *p*-type CNT-TFTs is completed.

Subsequently, to form *n*-type IGZO-TFTs, the 35-nm-thick IGZO film (In:Ga:Zn = 1:1:1 at. %) was deposited by radio frequency (RF) sputtering at 150 W in an argon and oxygen (Ar/O_2) mixture (3:0.1 sccm) at room temperature and patterned by a lift-off process. Then, Ti and gold (Au) layers (each 20 nm and 20 nm, respectively) were deposited using an e-beam evaporator to serve as the S/D electrodes, followed by a lift-off process. To open the gate contact pad, a photolithography process was performed, and the gate insulator (Al_2O_3/SiO_2) was wet-etched in a diluted hydrofluoric acid (HF) solution for 40 s. Next, 200-nm-thick SiO_2 was deposited by plasma enhanced chemical vapor deposition (PECVD) as an interlayer dielectric (ILD) layer, followed by wet etching in a diluted HF solution to open the S/D contact pads. Finally, Ti and Au layers (each 5 nm and 200 nm, respectively) were deposited with an e-beam evaporator as the metallization process for device-to-device interconnections; thus, hybrid CMOS ICs were completed.

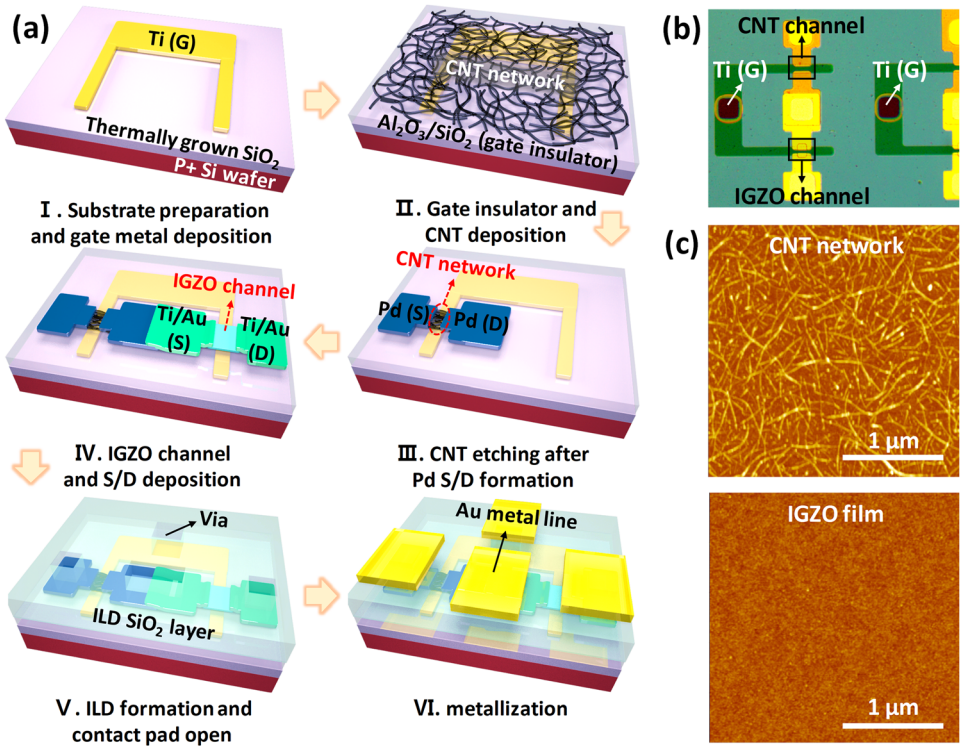

FIG. 1. (a) Process flow of the hybrid CMOS inverter. (I) Preparation of the starting Si wafer with a 300-nm-thick SiO_2 and deposition of a Ti local bottom gate electrode. (II) Formation of the semiconducting CNT network channel for *p*-type TFT fabrication after deposition of the Al_2O_3/SiO_2 gate insulator. (III) Deposition of *p*-type Ti/Pd S/D electrodes and CNT etching using oxygen plasma to define the semiconducting CNT channels. (IV) Sputtering of the IGZO channel to fabricate an *n*-type TFT and deposition of *n*-type Ti/Au S/D electrodes. (V) Formation of the SiO_2 ILD layer followed by contact pad opening. (VI) Au layer metallization process for interconnection between devices. (b) Optical micrograph image of the fabricated hybrid CMOS inverter based on *p*-type CNT- and *n*-type IGZO-TFTs. (c) AFM images of the CNT network channel and the IGZO thin film.

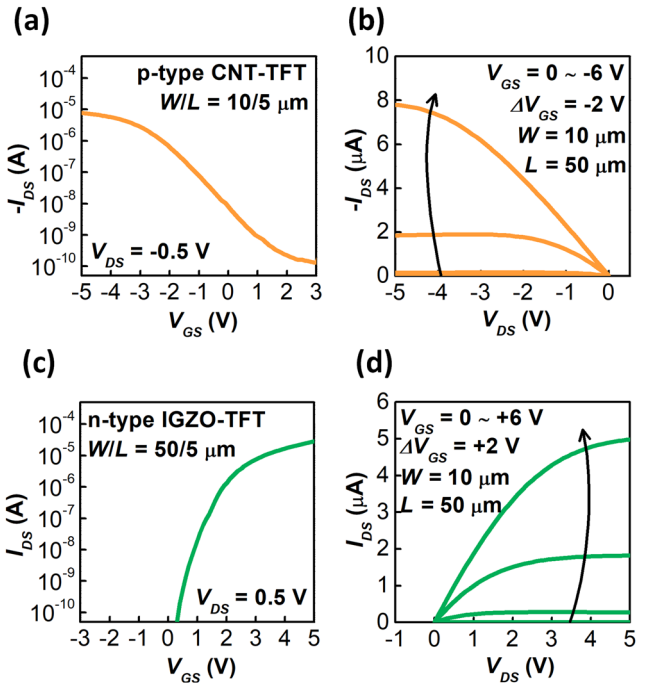

FIG. 2. (a) Transfer characteristics (I_{DS}–V_{GS}) of the *p*-type CNT-TFT with L = 5 μm and W = 10 μm composed of the 99% semiconducting CNT percolated network channel (deposition time of 20 min). (b) Output characteristics (I_{DS}–V_{DS}) of the CNT-TFT for different V_{GS} ranging from 0 V to −6 V in −2 V steps. (c) Transfer characteristics (I_{DS}–V_{GS}) of the *n*-type IGZO-TFT with L = 5 μm and W = 50 μm composed of the amorphous IGZO thin-film channel (oxygen flow rate of 0.1 sccm). (d) Output characteristics (I_{DS}–V_{DS}) of the IGZO-TFT for different V_{GS} values ranging from 0 V to 6 V in 2 V steps.

Figure 1(b) depicts the optical microscope image of the hybrid CMOS inverter. Atomic force microscopy (AFM) images of the 99% semiconducting CNT network and the IGZO thin film are shown in the channels of *p*-type and *n*-type TFTs, respectively. From the AFM images, it is confirmed that the CNT network channel and IGZO thin-film were uniformly formed across the entire area. The average CNT density obtained for 20 min deposition was extracted as 75 tubes/μm^2 ± 4 tubes/μm^2, and the surface roughness of the IGZO thin-film was 0.3 nm.

The defined channel lengths (L) and widths (W) in the fabricated CNT- and IGZO-TFTs ranged from 2 μm to 50 μm and from 2 μm to 50 μm, respectively. Figure 2(a) exhibits the transfer characteristics (i.e., drain current, $-I_{DS}$, vs gate voltage, V_{GS}) of the *p*-type CNT-TFTs with a W of 10 μm and an L of 5 μm at a drain voltage (V_{DS}) of −0.5 V. The measured CNT-TFTs appear to operate with good *p*-type behavior. The key metrics of the CNT-TFTs, such as normalized I_{ON}, i.e., $-I_{ON} \times L/W$ (I_{ON} of the CNT-TFTs is defined at V_{GS} = −5 V and V_{DS} = −0.5 V), log(I_{ON}/I_{OFF}) (the off-state current, I_{OFF}, is defined at V_{GS} = 3 V and V_{DS} = −0.5 V), and μ_{FE}, were determined to be 3.31 μA ± 0.75 μA, 4.72 cm^2/V s ± 0.28 cm^2/V s, and 45.2 cm^2/V s ± 7.4 cm^2/V s, respectively. The μ_{FE} of CNT-TFTs was determined using the current–voltage equation and by calculating a sophisticated cylindrical model.[31] The representative output characteristics (i.e., $-I_{DS}$ vs V_{DS}) of the CNT-TFTs at various V_{GS} values are shown in Fig. 2(b). Furthermore, semiconducting CNT-TFTs present clear I_{DS} saturation behavior, as shown in the output characteristics. Importantly, these curves appear to be linear at small V_{DS} values, indicating that ohmic contact is well formed between the Pd S/D and the CNT networks. In addition, Figs. 2(c) and 2(d) show the transfer and output characteristics of the *n*-type IGZO-TFTs with a W of 50 μm and an L of 5 μm at a V_{DS} of 0.5 V. The typical $I_{ON} \times L/W$ defined at V_{GS} = 5 V, the log(I_{ON}/I_{OFF}) (I_{OFF} of the IGZO-TFTs is defined at V_{GS} = −3 V), and μ_{FE} were extracted as 3.24 μA ± 0.91 μA, 5.95 cm^2/V s ± 0.85 cm^2/V s, and 23.3 cm^2/V s ± 4.5 cm^2/V s, respectively. We confirmed the good saturation behavior of the IGZO-TFTs, with ohmic contacts between the Ti/Au S/D and the IGZO thin-film as well. As a result, as shown in the output characteristics, the electrical performance of the CNT- and the IGZO-TFTs is not symmetrical; hence, the device geometry of the CNT-TFT with W/L = 10/5 μm and that of the IGZO-TFT with W/L = 50/5 μm were chosen as the optimized conditions used in the hybrid CMOS ICs.

Figure 3(a) shows a schematic diagram of a hybrid CMOS inverter based on *p*-type CNT- and *n*-type IGZO-TFTs. Figure 3(b) demonstrates the voltage transfer curves (VTCs) of the hybrid CMOS inverter with supply voltages (V_{DD}) of 4 V, 6 V, 8 V, and 10 V. The hybrid CMOS inverter exhibits sharp switching with rail-to-rail output voltage (V_{OUT}) behavior. The logic threshold voltages (V_{LT}) of the hybrid CMOS inverter where the input voltage (V_{IN}) equals V_{OUT} were measured close to V_{DD}/2 due to the optimized device dimensions of the CNT- and IGZO-TFTs. The voltage gains of our hybrid CMOS inverter are 36 V/V, 59 V/V, 70 V/V, and 123 V/V with V_{DD} values of 4 V, 6 V, 8 V, and 10 V, respectively. These results show higher voltage gains at lower V_{DD} than the previously reported hybrid CMOS inverters based on CNT- and IGZO-TFTs[23,24] due to our optimized process conditions. By controlling the device dimensions and process conditions, we were able to achieve the enhanced performances, regarding log(I_{ON}/I_{OFF}), μ_{FE}, and I_{ON}, which also

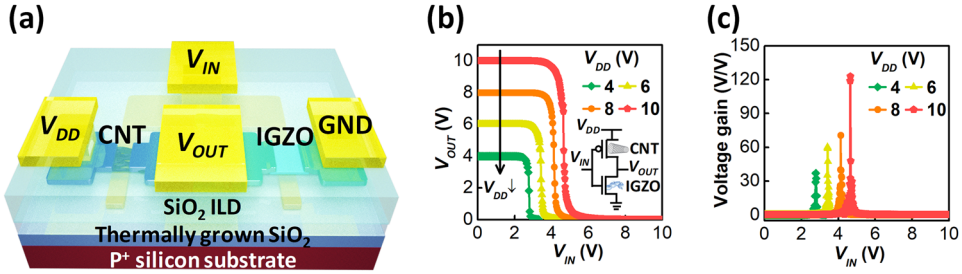

FIG. 3. (a) A schematic diagram of a hybrid CMOS inverter consisting of *p*-type CNT- and *n*-type IGZO-TFTs. (b) Voltage transfer characteristics (VTCs) of the hybrid CMOS inverter obtained at V_{DD} from 4 V to 10 V by a 2 V step. The inset is an equivalent circuit of a hybrid CMOS inverter. (c) Voltage gain of the hybrid CMOS inverter depending on V_{DD}.

TABLE I. Performance comparison for the CNT- and IGZO-TFTs and hybrid CMOS inverter.

References	*p*-type CNT-TFT				*n*-type IGZO-TFT				Supply voltage (V_{DD}) (V)	Inverter gain	Power consumption (μW)
	$-I_{ON} \times W/L$ (μA)	Log (I_{ON}/I_{OFF})	V_T (V)	μ_{FE} (cm^2/V s)	$I_{ON} \times W/L$ (μA)	Log (I_{ON}/I_{OFF})	V_T (V)	μ_{FE} (cm^2/V s)			
This work	3.92	4.78	−1.1	48.7	3.38	6.62	1.2	20.7	4	36	0.06
									6	59	0.87
									8	70	3.4
									10	123	9.8
16	2	5	−12	11.7	7	5.8	2.5	12.9	20	109	20
23	1.2	6	−2	15	2.83	6	1.2	8	5	20.9	1.8
24	0.2	5	−2	6	1	5	3	4.93	5	45	0.6

resulted in the enhanced voltage gain of the hybrid CMOS inverter.[16] In addition, the maximum power consumption of the fabricated hybrid CMOS inverter is 9.8 μW at a V_{DD} of 10 V, which indicates low power consumption of our hybrid CMOS inverter. The key metrics of the mentioned CNT- and IGZO-TFTs and hybrid CMOS inverter composed of them are quantitatively summarized in Table I.

Figure 4(a) presents a schematic illustration of a two-input hybrid NOR gate implemented based on *p*-type CNT- and *n*-type IGZO-TFTs. The NOR gate is realized by connecting two CNT-TFTs in series and two IGZO-TFTs in parallel. The NOR gate demonstrates a rail-to-rail voltage swing from 0 V to 10 V at a V_{DD} of 10 V. Figure 4(b) shows the output of the NOR gate that correctly returns the output of logic "1" state (10 V) only at the condition when both of the inputs (V_A and V_B) are set to logic "0" state (0 V) or when both IGZO-TFTs are turned off. Figure 4(c) shows a schematic circuit diagram of the NAND gates, which are achieved by connecting two CNT-TFTs in parallel and two IGZO-TFTs in series. Figure 4(d) also illustrates the output of the NAND gate returning correctly a signal logic "0" state (0 V) only when both of the inputs are logic "1" state (10 V) or when both CNT-TFTs are turned off. Logic circuits such as NAND and NOR gates return accurate output signals based on their input logics, which are some of the basics in modern digital IC. This allows the design of hybrid CMOS ICs to further explore the possibilities of implementing high-performance digital logic circuits.

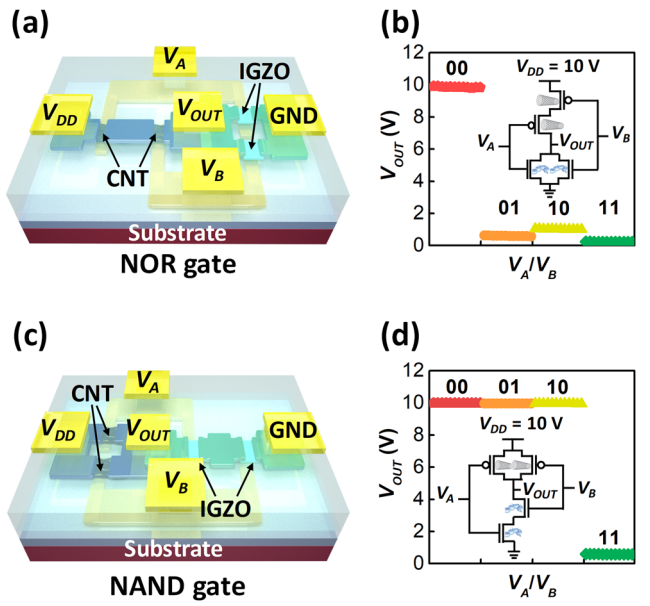

FIG. 4. (a) A schematic diagram of a two-input hybrid NOR logic gate consisting of two CNT-TFTs in series and two IGZO-TFTs in parallel. (b) Output characteristics of the hybrid NOR gate at V_{DD} = 10 V. The inset is an equivalent circuit of a two-input hybrid NOR logic gate. (c) A schematic diagram of a two-input hybrid NAND logic gate consisting of two CNT-TFTs in parallel and two IGZO-TFTs in series. (d) Output characteristics of the hybrid NAND gate at V_{DD} = 10 V. The inset is an equivalent circuit of a two-input hybrid NAND logic gate.

In conclusion, we demonstrated a hybrid integration based on *p*-type CNT- and *n*-type IGZO-TFTs to implement hybrid CMOS ICs. Individual CNT- and IGZO-TFTs with high I_{ON}, high log(I_{ON}/I_{OFF}), and high μ_{FE} were fabricated, and the two TFTs exhibited balanced electrical performance. Furthermore, by employing these TFTs, we implemented a hybrid CMOS inverter with high voltage gain and low power consumption. We also show the operations of the two-input NOR and NAND logic gates fabricated with a combination of CNT- and IGZO-TFTs. As a result, the NOR and NAND gates return correct logical functions according to input signals. We believe that our approach of hybrid integration of CNT- and IGZO-TFTs offers great improvement for various macroelectronic applications.

This work was supported by the National Research Foundation (NRF) of Korea under Grant Nos. 2019R1A2B5B01069988 and 2016R1A5A1012966 and by the Future Semiconductor Device Technology Development Program (Grant No. 10067739) funded by MOTIE (Ministry of Trade, Industry & Energy) and KSRC (Korea Semiconductor Research Consortium).

REFERENCES

[1] D.-H. Kim, N. Lu, R. Ma, Y.-S. Kim, R.-H. Kim, S. Wang, J. Wu, S. M. Won, H. Tao, A. Islam *et al.*, Science **333**, 838 (2011).
[2] A. Chortos, J. Lu, and Z. Bao, Nat. Mater. **15**, 937 (2016).

[3]J. Yoon, B. Choi, Y. Lee, J. Han, J. Lee, J. Park, Y. Kim, D. M. Kim, D. H. Kim, M.-H. Kang, S. Kim, and S.-J. Choi, in *IEEE International Electron Devices Meeting (IEDM)* (IEEE, 2017), p. 40.2.1.
[4]S.-J. Park, J. Kim, M. Chu, and M. Khine, Adv. Mater. **3**, 1700158 (2017).
[5]M. Yu, H. Wan, L. Cai, J. Miao, S. Zhang, and C. Wang, ACS Nano **12**, 11572 (2018).
[6]J. B. Andrews, J. A. Cardenas, C. J. Lim, S. G. Noyce, J. Mullett, and A. D. Franklin, IEEE Sens. J. **18**, 7875 (2018).
[7]C. Zhao, D. Zhong, J. Han, J. Liu, Z. Zhang, and L.-M. Peng, Adv. Funct. Mater. **9**, 1808574 (2019).
[8]Y. Lee, J. Yoon, B. Choi *et al.*, Appl. Phys. Lett. **111**, 173108 (2017).
[9]B.-W. Wang, S. Jiang, Q.-B. Zhu, Y. Sun, J. Luan, P.-X. Hou, S. Qiu, Q.-W. Li, C. Liu, D.-M. Sun, and H.-M. Cheng, Adv. Mater. **30**, 1802057 (2018).
[10]H. Zhang, L. Xiang, Y. Yang, M. Xiao, J. Han, L. Ding, Z. Zhang, Y. Hu, and L.-M. Peng, ACS Nano **12**, 2773 (2017).
[11]D. Zhong, Z. Zhang, L. Ding, J. Han, M. Xiao, J. Si, L. Xu, C. Qiu, and L.-M. Peng, Nat. Electron. **1**, 40 (2017).
[12]Y. Lee, H. Jung, B. Choi, J. Yoon, H. B. Yoo, H.-J. Kim, G.-W. Park, D. H. Kim, D. M. Kim, M.-H. Kang, and S.-J. Choi, RSC Adv. **9**, 22124 (2019).
[13]M. S. Arnold, A. A. Green, J. F. Hulvat, S. I. Stupp, and M. C. Hersam, Nature **1**, 60 (2006).
[14]N. Moriyama, Y. Ohno, T. Kitamura, S. Kishimoto, and T. Mizutani, Nanotechnology **21**, 165201 (2010).
[15]P. Avouris, Acc. Chem. Res. **35**, 1026 (2002).
[16]J. Yoon, H. Jung, J. T. Jang, J. Lee, Y. Lee, M. Lim, D. M. Kim, D. H. Kim, and S.-J. Choi, J. Alloys Compd. **762**, 456 (2018).
[17]D. Shahrjerdi, A. D. Franklin, S. Oida, J. A. Ott, G. S. Tulevski, and W. Haensch, ACS Nano **7**, 8303 (2013).
[18]Y. Yang, J. Han, Z. Zhang, and L.-M. Peng, ACS Nano **11**, 4124 (2017).
[19]J. Lee, J. Yoon, B. Choi, D. Lee, D. M. Kim, D. H. Kim, Y.-K. Choi, and S.-J. Choi, Appl. Phys. Lett. **109**, 263103 (2017).
[20]J. Zhang, C. Wang, Y. Fu, Y. Che, and C. Zhou, ACS Nano **5**, 3284 (2011).
[21]J. H. Koo, S. Jeong, H. J. Shim, D. Son, J. Kim, D. C. Kim, S. Choi, J.-I. Hong, and D.-H. Kim, ACS Nano **11**, 10032 (2017).
[22]T. Lei, L.-L. Shao, Y.-Q. Zheng, G. Pitner, G. Fang, C. Zhu, S. Li, R. Beausoleil, H.-S. P. Wong, T.-C. Huang, K.-T. Cheng, and Z. Bao, Nat. Commun. **10**, 2161 (2019).
[23]H. Chen, Y. Cao, J. Zhang, and C. Zhou, Nat. Commun. **5**, 4097 (2014).
[24]W. Honda, S. Harada, S. Ishida, T. Arie, S. Akita, and K. Takei, Adv. Mater. **27**, 4674 (2015).
[25]Y. Li, J. Zhang, J. Yang, Y. Yuan, Z. Hu, Z. Lin, A. Song, and Q. Xin, IEEE Trans. Electron Devices **66**, 950 (2019).
[26]S. Choi, J.-Y. Kim, J. Rhee, H. Kang, S. Park, D. M. Kim, S.-J. Choi, and D. H. Kim, IEEE Electron Device Lett. **40**, 574 (2019).
[27]J. C. Park, S. Kim, S. Kim, C. Kim, I. Song, Y. Park, U.-I. Jung, D. H. Kim, and J.-S. Lee, Adv. Mater. **22**(48), 5512 (2010).
[28]J. S. Park, W.-J. Maeng, H.-S. Kim, and J.-S. Park, Thin Solid Films **520**, 1679 (2012).
[29]Y. Lee, B. Choi, J. Yoon, Y. Kim, J. Park, H.-J. Kim, D. H. Kim, D. M. Kim, S. Kim, and S.-J. Choi, AIP Adv. **8**, 065109 (2018).
[30]J. Yoon, J. Han, B. Choi, Y. Lee, Y. Kim, J. Park, M. Lim, M.-H. Kang, D. H. Kim, D. M. Kim, S. Kim, and S.-J. Choi, ACS Nano **12**, 6006 (2018).
[31]Q. Cao, M. Xia, C. Kocabas, M. Shim, and J. A. Rogers, Appl. Phys. Lett. **90**, 023516 (2007).